Visualization of velocity fields in the atmosphere from the scattered radiation

V.A. Banakh and A.V. Falits

V.E. Zuev Institute of Atmospheric Optics, Siberian Branch of the Russian Academy of Sciences, Tomsk

Received April 17, 2008

Possibilities of 2D velocity field visualization in the atmosphere with the help of the laser radiation scattered by particles, which move in a turbulent air flow, have been analyzed. With the aid of numerical simulation, it is demonstrated that the visualization of the flow velocity field is possible based on displacements of large-scale intensity inhomogeneities in the speckle structure, arising in the optical image of the scattering layer region illuminated by a laser.

Introduction

By the principle of measurement, the known methods of remote laser determination of liquid or gas flow rates[1–5] can be divided into two groups. One of them consists of methods based on measuring the Doppler frequency shift of the scattered laser radiation. The Doppler shift is connected with the velocity of scattering particles entrained by a flow. This allows the longitudinal (with respect to the sensing rate) component of the flow rate to be determined with a high accuracy. If the flow velocity is inhomogeneous, then measurements with the use of laser Doppler anemometers should be conducted in different parts of the flow.

The second group of widely used methods for measuring and visualizing the velocity field in gas and liquid flows is based on recording either coherent images of particles groups in a flow (particle image velocimetry (PIV)) or the speckle structure of the field, scattered by these particles (laser speckle photography or speckle interferometry), followed by the correlation analysis of pairs of images recorded at different instants. These methods rank below the Doppler velocity measurements in accuracy or give only a qualitative pattern of the velocity field in a flow. However, they provide for the real-time information on the dynamics of the flow as a whole, rather than its parts, as in the case of Doppler anemometers.

The application of these methods to determination of the velocity assumes the presence of particles, which are entrained by the flow and scatter radiation. To do this, the flow under study is artificially sown with scattering particles. Of importance are identical sizes of the particles and their homogeneous concentration in the flow.

Doppler laser velocity meters (lidars) are successfully used for determination of the wind velocity in the atmosphere, in which the particles of natural atmospheric aerosol play the role of scatterers. At the same time, for some problems, for example, indication of areas with increased turbulence or vortex and coherent structures in the atmosphere, methods providing for real-time visualization of the velocity field in extended areas are more attractive. In particular, in Ref. 6 PIV setups were used in bench measurements for visualization of the velocity field of air flows generated by a helicopter propeller. However, for atmospheric problems the direct use of finished PIV or speckle technologies faces great difficulties, since it is practically impossible to obtain images of aerosol particles at many-kilometer paths for analysis of their motion in space, and the observed dynamics of speckles, resolved at such distances, does not reflect the actual motion of the air flow in the atmosphere.

The possibility of visualization of the velocity field from the laser radiation, reflected in the turbulent atmosphere, is discussed in Refs. 7–9, in which aerosol particles are not considered as tracers, but as scatterers in a layer, which form a diffuse surface, homogeneously reflecting the radiation. The velocity field was visualized in Refs. 7–9 from shifts of random intensity inhomogeneities in the cross section of the laser beam incident on a reflecting aerosol layer. It was assumed that shifts of spatial inhomogeneities of the laser beam are caused by the motion of turbulent inhomogeneities of the refractive index entrained by the air flow on the propagation path of the illuminating radiation.

In Refs. 10 and 11, the air flow was experimentally visualized through correlation processing of pairs of images of the laser spot, resulted in the atmosphere from light scattering by snow particles, artificial CO_2 fog, and refractive index inhomogeneities.

This paper presents the computer model, imitating the experiments.[10, 11] In contrast to Refs. 7–9, the visualization of the velocity field here is based on the separation of large-scale inhomogeneities in the intensity distribution in the image of the illuminated layer. These inhomogeneities are not caused by the turbulence of the air refractive

0235-6880/08/10 775-07 $02.00

index, but by scattering of laser radiation by particles moving in accordance with the velocity field of the flow under study.

In other words, in Eq. (20) of Ref. 9 we should replace the homogeneous distribution of scattering particle positions in the refracting layer with the distribution, depending functionally on the velocity field in the flow. Possibilities of the velocity field visualization from the scattered radiation are analyzed here through consecutive simulation of the illuminating beam in the process of propagation, reflection, and image formation, rather than with the use of the integral relationship determining the intensity in the image plane through the intensities of the illuminating and scattered beams [Eq. (13) in Ref. 9]. Turbulent fluctuations of the air refractive index were neglected in the simulation.

1. Algorithm for visualization of the velocity field in the atmosphere

Figure 1 illustrates propagation of the illuminating radiation and formation of the image of an illuminated object. A coherent collimated Gaussian beam passes to the reflecting layer, where it is scattered by aerosol particles. The scattered radiation propagates in the backward direction and is collected by a lens, behind which the image is formed.

In the reflection plane, the complex amplitude of the scattered field U is formed as a 2D array of complex values at nodes of the computational grid according to the equation

$$U_{n,m} = U^G_{n,m} U^R_{n,m}, \quad (1)$$

where n and m are indices of the nodes, at which U^G is the array of values of the field of the illuminating beam in the reflection plane; U^R is the array of values of the function simulating the field scattering at aerosol particles. The array U^R is determined by the equation

$$U^R_{n,m} = A_{n,m} \exp[i\varphi_{n,m}], \quad (2)$$

where A and φ are the arrays of values of the amplitude and phase of the complex parameter, which are random functions, whose values are distributed uniformly from 0 to 1 and from 0 to 2π, respectively. The array of values of $\varphi_{n,m}$ simulates random changes in the phase of the illuminating wave due to the random arrangement of scattering particles, while the array of values of $A_{n,m}$ simulates the random scattering amplitude of particles.[12,13]

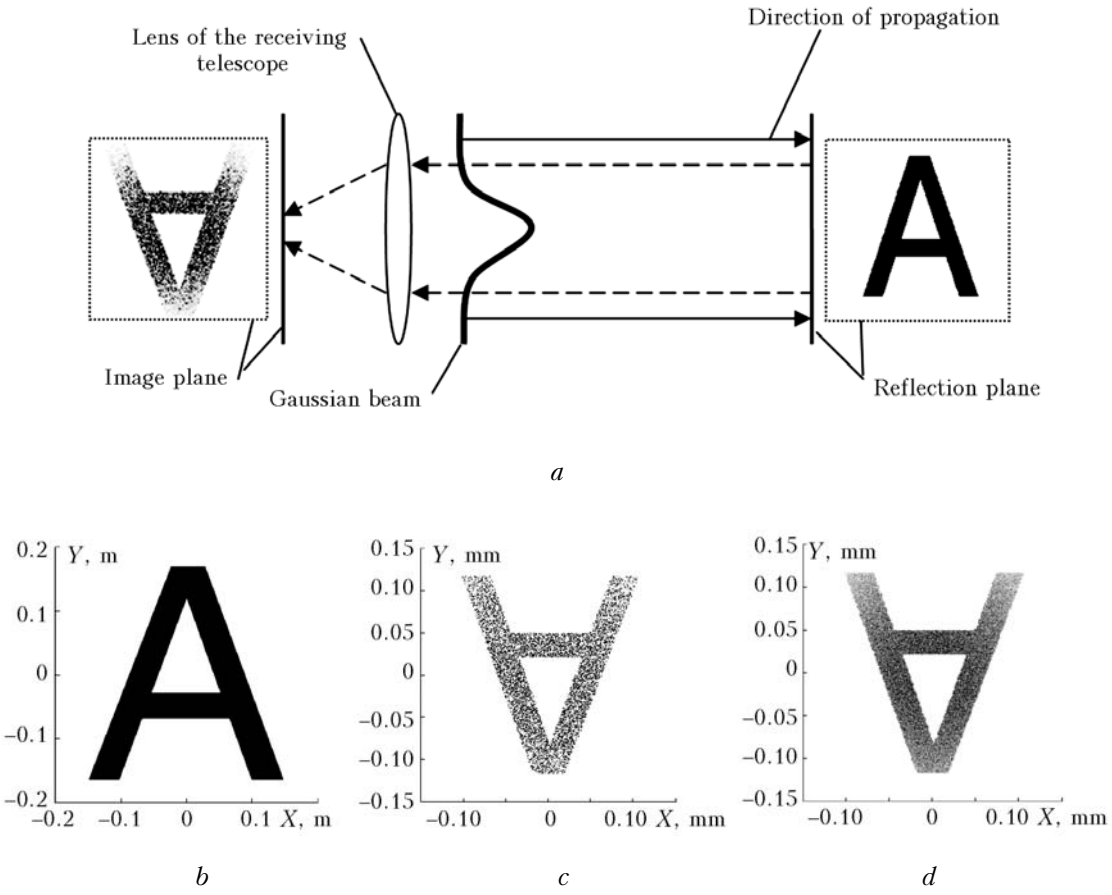

Fig. 1. Block diagram of the numerical experiment (*a*), model of the observed object (*b*), its coherent image (*c*), and coherent image averaged over 25 realizations (*d*).

Propagation of the scattered field from the reflection plane to the lens of the receiving telescope was simulated with the use of the Fast Fourier Transform algorithm[14]

$$U^L_{n,m} = FFT^{-1}\left[FFT[U_{n,m}]\exp\left(\frac{-i\pi\lambda L}{h^2}(m^2+n^2)\right)\right], \quad (3)$$

where $U^L_{n,m}$ is the 2D array of values of the complex amplitude of the reflected field in the objective plane; λ is the wavelength; L is the length of the propagation path; h is the distance between nodes of the computational grid; $FFT[\,]$ and $FFT^{-1}[\,]$ stand for direct and inverse Fourier transforms.

The intensity distribution of the scattered field in the plane of the sharp image of the receiving telescope U^l was calculated as

$$U^l_{n,m} = \frac{h^2}{\lambda i l}\exp\left\{\frac{i\pi h'^2}{\lambda l}\left(n^2+m^2\right)\right\}\times$$

$$\times FFT\left[T_{n,m}U^L_{n,m}\exp\left(\frac{i\pi h^2}{2\lambda}\left(\frac{1}{l}-\frac{1}{f}\right)\left(n^2+m^2\right)\right)\right], \quad (4)$$

where l is the distance from the objective to the plane of the sharp image; f is the focal length of the receiving telescope; h' is the distance between nodes of the computational grid in the image plane; $T_{n,m}$ is the array of values of the objective transmission function. The distance between the lens and the plane of the sharp image is determined by the relation

$$\frac{1}{L}+\frac{1}{l}=\frac{1}{f}.$$

In contrast to photographies in white light, coherent images include speckles.[2] Figure 1 shows the model regular distribution of the amplitude of the scattered field $A_{n,m}$ in Eq. (2), the image of this distribution obtained in coherent light, and the result of averaging of coherent images of the distribution over 25 realizations. At the random reflection coefficient of particles, the image of the laser spot on the scattering layer is even more contrast.[2] Just the speckle structure of coherent images necessitates the building of computer models for analysis of the possibility of the velocity field visualization in the atmosphere from the scattered laser radiation.

Temporal changes of the intensity distribution in the image of the illuminated fragment of the reflecting layer are determined from motion of scattering particles entrained by the air flow. We assume that the flow velocity vector in the transverse (to the illuminating beam direction) plane can be represented as a sum of the regular (mean) velocity and the fluctuation component, caused by the turbulent mixing of scattering particles. Then, for the velocity at grid nodes $\mathbf{V}_{n,m}$ we obtain

$$\mathbf{V}_{n,m} = \mathbf{V}^M_{n,m} + \mathbf{V}^F_{n,m}, \quad (5)$$

where $\mathbf{V}^M_{n,m}$ and $\mathbf{V}^F_{n,m}$ are the regular velocity and the fluctuation component.

In simulation, it was assumed that the regular velocity field in the flow is circular with the linear increase of the tangential velocity along the circle radius from zero to some maximal value. In this way, we imitated the change of the regular flow velocity both in the absolute value and in the direction.

The regular velocity in numerical simulation was specified by circular motion of scattering particles around the center of the reflection plane. For the specified distribution of the velocity field, the distances, to which scattering particles move, depend on time between fixations of their positions. As an example, figure 2*a* shows the initial arrangement of particles (marked by o) and their positions 20 ms later (marked by •) for a maximal flow velocity of 1 m/s.

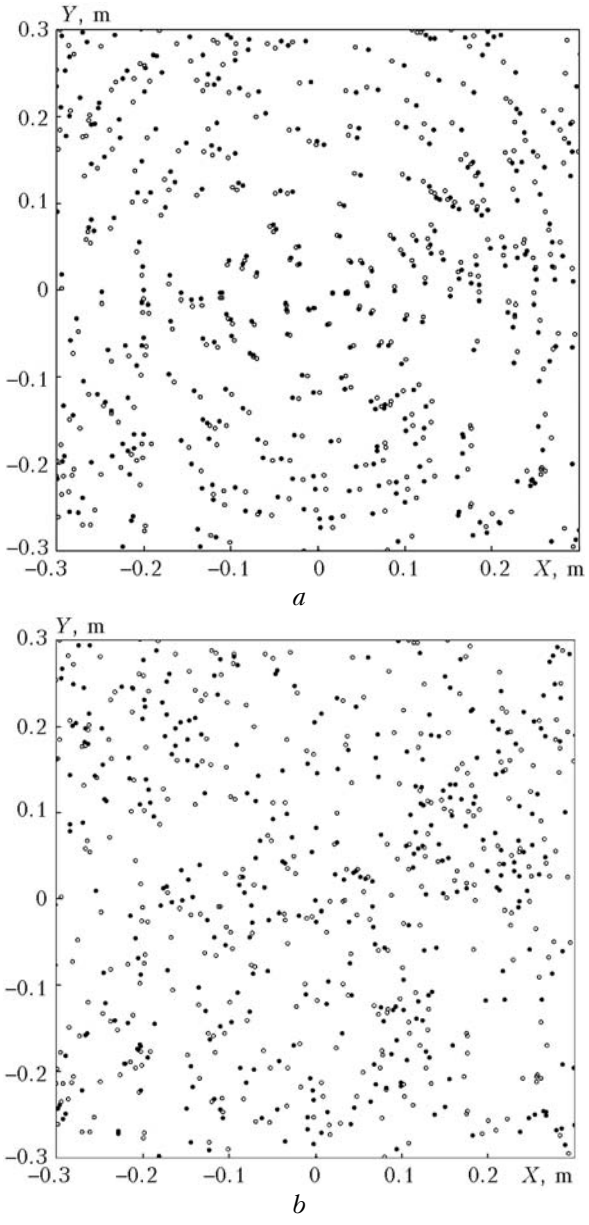

Fig. 2. Displacement of scattering particles with the mean velocity (*a*) and as a result of turbulent fluctuations of the wind velocity (*b*).

Fluctuations of the flow velocity in the atmosphere were modeled by the two-dimensional Karman model of turbulence.[15,16] Fluctuations of wind velocity in this model are homogeneous, isotropic, and determined by the "8/3-law" spatial spectrum of inhomogeneities, which includes the velocity dispersion and outer scale of turbulence as parameters. Figure 3 exemplifies 2D distributions of the coordinate components of the fluctuation component of the wind velocity vector $\mathbf{V}^F = (V_x^F, V_y^F)$, obtained for dispersion of velocity fluctuations equal to 1 m^2/s^2 and an outer scale of 1 m.

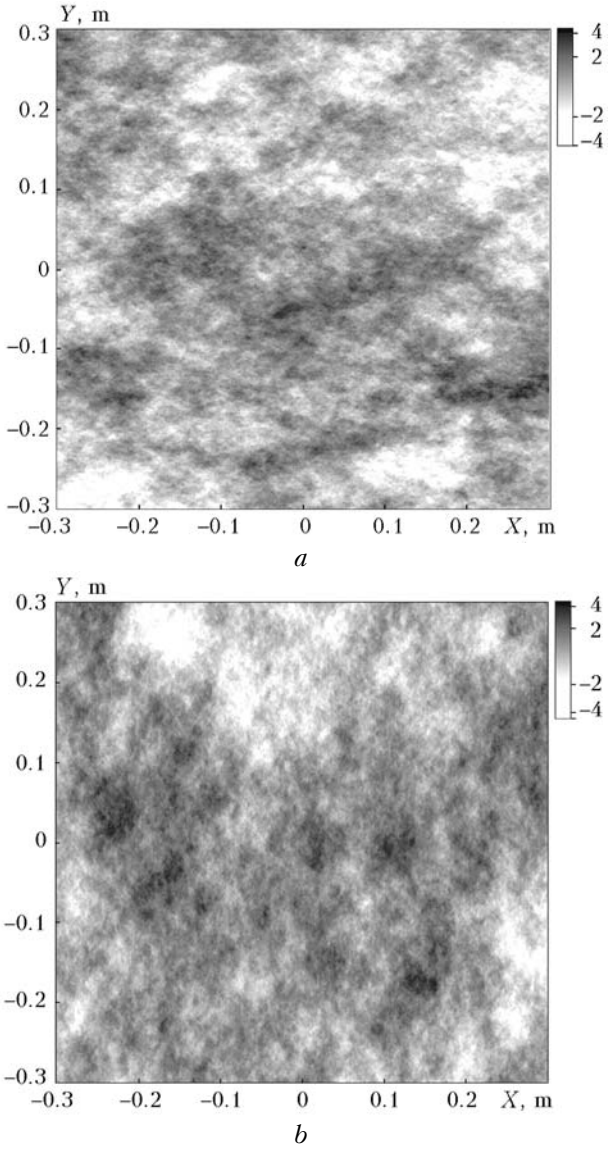

Fig. 3. Components of the vector of random component of the flow velocity: (*a*) component V_x^F; (*b*) component V_y^F.

Figure 2*b* shows initial positions of particles and their arrangement, as in Fig. 2*a*, 20 ms later. Random wandering of every particle during this time was modeled according to realizations of the fields of components of the random velocity vector, which are exemplified in Fig. 3.

For comparative analysis of intensity distributions in images of the illuminated spot on the scattering layer obtained at different instants, the difference between which is determined by displacements of scattering particles entrained by the flow, the iterating procedure was developed. Areas of certain dimension (squares, Fig. 4) are separated from the analyzed intensity distributions and then the sums of square differences between separated image areas are calculated:

$$\mathrm{Sum}(j,q) = \sum_{k,g} (I^{(1)}_{n+k,m+g} - I^{(2)}_{n+k+j,m+g+q})^2, \qquad (6)$$

where $I^{(1)}$ and $I^{(2)}$ are intensities in the images obtained at different instants; k and g are indices of the array of intensity values for the fragment separated from the general distribution; j and q are indices of displacement of the separated 2D array.

At the first step, the sums of square differences of intensities with identical indices in the separated arrays, that is, at $j = q = 0$ have been calculated. Then the sums are calculated of square differences between intensities after displacement of the separated fragment by 1 pixel in different directions in one of the distributions. The minimal value of the calculated sums

$$\mathrm{Min}[\mathrm{Sum}(0,0), \mathrm{Sum}(-1,0), \mathrm{Sum}(1,0), \mathrm{Sum}(0,-1), \mathrm{Sum}(0,1)] \qquad (7)$$

indicates the direction of the separated fragment of the image. If the indices of displacement for the minimal calculated sum are nonzero, then the procedure is repeated with zero indices of displacement, assigned to the minimal sum of square intensity differences. Iterations are performed until the minimal calculated sum (6) becomes the sum with zero values of displacement indices, that is, Sum(0,0). This means that a fragment with minimal intensity deviations from the separated fragment in the first image is found in the second image. The direction of displacement of each of separated areas in the second image relative to the first image just determines the structure of the velocity field causing these displacements.

Figure 4 shows the intensity distributions in the image of the illuminated fragment of the reflecting layer for the arrangements of scattering particles shown in Fig. 2*a*. Analysis of displacements of different image areas for the time between measurements by the procedure (6), (7) allows the visualization of the velocity field in the flow (shown by arrows in Fig. 4*b*). Application of the correlation methods of the image comparison commonly used in PIV [Ref. 4] to these intensity distributions gives a worse visualization than that shown in Fig. 4*b*. Algorithm (6), (7) also turned to be more stable than the PIV correlation methods of visualization in other numerical experiments considered in this paper.

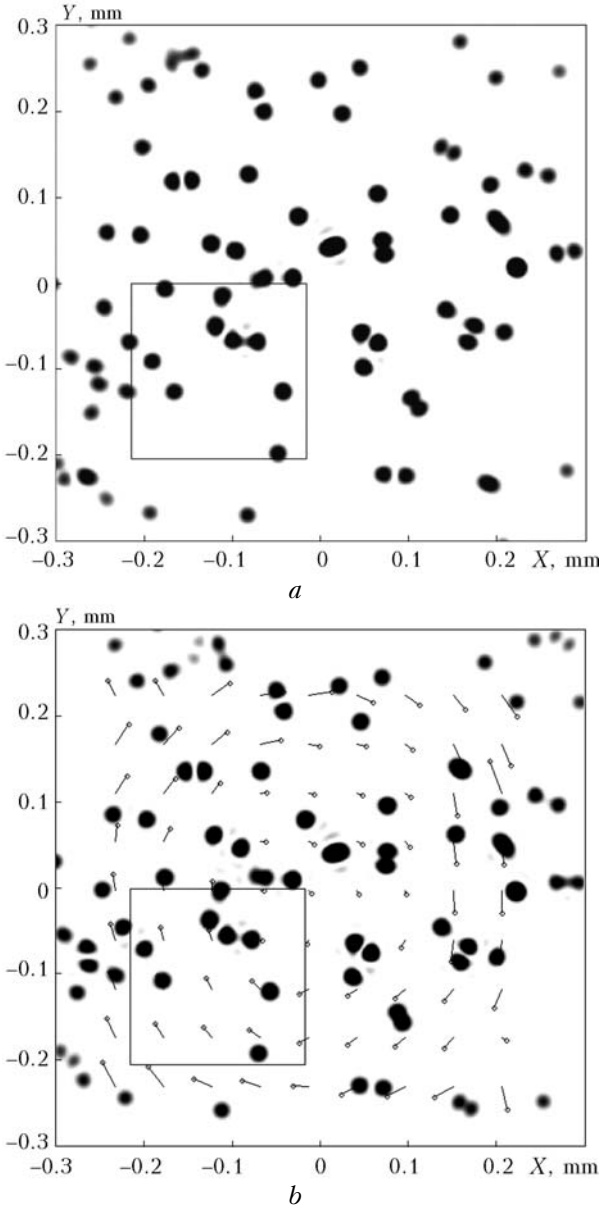

Fig. 4. Intensity distributions in the image of the illuminated fragment obtained for the positions of scattering particles shown in Fig. 2*a* and results of visualization of the velocity field.

2. Results of simulation

The following numerical scheme is considered (see Fig. 1). A Gaussian optical beam with an initial radius $R_b = 0.15$ m and the wavelength $\lambda = 0.57$ μm propagates along a path of the length $L = 500$ m. At the path end, the beam scatters at a particle layer. The backward radiation after propagation of the path is collected by a lens of the diameter $D_t = 0.2$ m and the focal length $f = 1$ m. The beam propagation was simulated at an $N_x \times N_y = 1024 \times 1024$ array of values of the complex field, and a step of the computational grid h for the field was $0.72 \cdot 10^{-3}$ m. A step of the computational grid in the image plane h' was $0.72 \cdot 10^{-6}$ m. The time between measurements, during which scattering particles, entrained by the flow, displace, was set equal to 0.02 s. The sizes of arrays to be separated from the initial arrays of intensity values in images for analysis of displacements of different image areas were taken $N_x \times N_y = 256 \times 256$ pixels. Sixty four overlapping areas in an image were considered.

Figure 5*a* shows the resultant intensity distribution in the image of the illuminated fragment in the reflecting layer, which was formed by scattering particles moving in the velocity field of the air flow with the maximal regular velocity $V^M_{\max} = 0.2$ m/s in the absence of fluctuations ($V^F = 0$), and the results of visualization of the velocity field in the flow by the algorithm (6), (7).

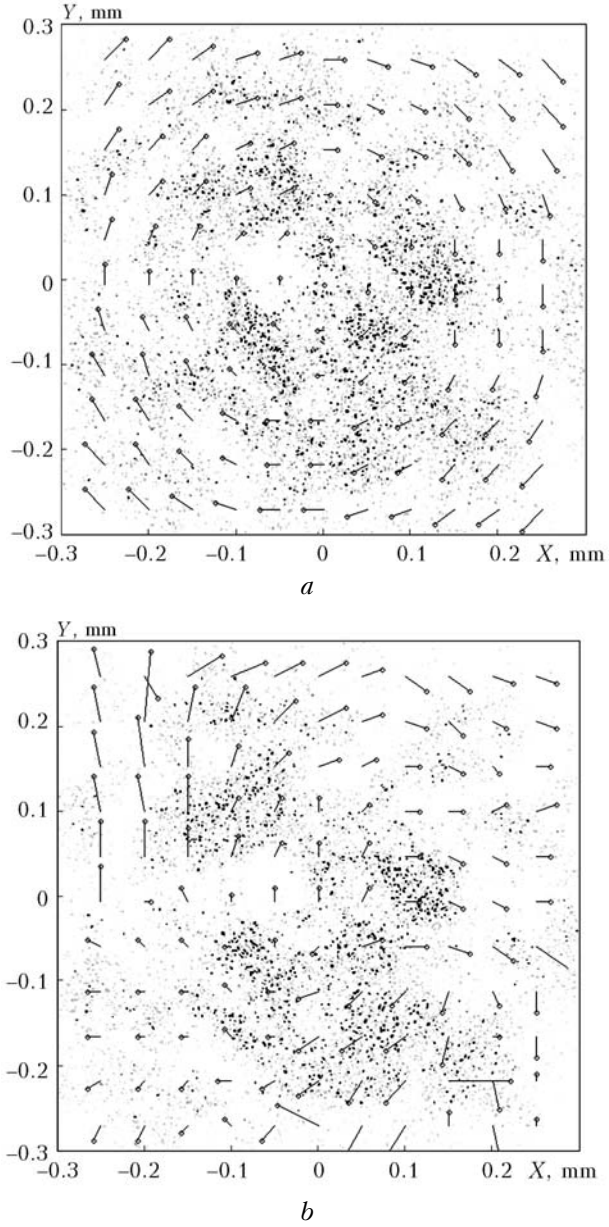

Fig. 5. Visualization of the velocity field from the speckle structure of images.

It can be seen from Fig. 5*a* that the intensity distribution in the image is a small-scale speckle structure against the background of larger-scale intensity inhomogeneities, and the visualized pattern well reconstructs the circular velocity field in the flow. Large-scale intensity inhomogeneities appear due to clusterization of scattering particles[17] because of their random arrangement in space (2) in the analyzed pairs of images.

If the regular velocity field in the flow is supplemented with the fluctuation component $\mathbf{V}^F \neq 0$, that is, the regular circular displacement of every particle is supplemented with random wandering, then the visualization of the regular flow motion, as follows from Fig. 5*b*, becomes nearly impossible. Figure 5*b* shows the results of simulation of the intensity distribution in the image and the visualized pattern of the velocity field for $V^M_{\max} = 0.2$ m/s and the turbulence parameters specified in simulation of random components of the wind velocity, which are exemplified in Fig. 3. The visualization becomes impossible, because due to turbulent mixing of scattering particles the speckle structure of the image "boils up," thus causing statistical independence of small-scale intensity distributions in analyzed pairs of images. In this case, the distribution of large-scale intensity inhomogeneities in the image mostly keeps its structure.

The problem of visualization can be solved based on large-scale intensity fluctuations in images of the scattering layer. For this purpose, small-scale intensity fluctuations, determined by the speckle structure of the image, should be filtered out. Speckle filtering was performed through averaging of intensity values at some image pixels based on intensity values at neighboring pixels:

$$I_{n,m} = \frac{I_{n+1,m} + I_{n-1,m} + I_{n,m+1} + I_{n,m-1}}{4}, \qquad (8)$$

where the subscripts n and m determine nodes of the computational grid. The averaging procedure (8) is repeated by iterations until the influence of the speckle structure on the intensity distribution in the image is eliminated.

Figure 6*a* shows the result of iterative averaging of the intensity distribution shown in Fig. 5*b* and the following visualization of the velocity field based on the averaged images.

It is seen that the procedure failed to reconstruct specified circular velocity field from the averaged intensity distributions as well, because in the considered case the maximal regular flow velocity $V^M_{\max} = 0.2$ m/s was lower than the dispersion of velocity fluctuations (1 m/s).

Figure 6*b* shows the averaged intensity distributions in the image for the same model of the velocity field and for the same velocity fluctuations as in Fig. 6*a*, but for the maximal regular velocity $V^M_{\max} = 3$ m/s. It also shows the results of visualization of the velocity field through processing of averaged intensity distributions by algorithm (6), (7). It can be seen that in this case the specified circular velocity field is reconstructed distinctly.

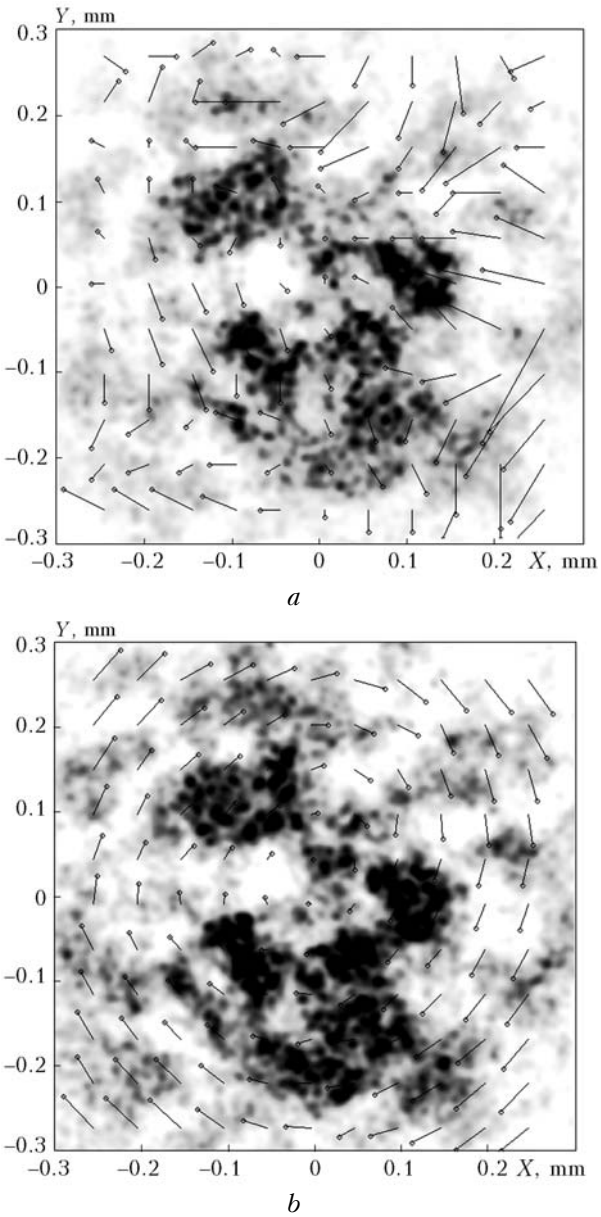

Fig. 6. Visualization of the velocity field based on averaged intensity distributions in images of the scattering layer $V^M_{\max} = 0.2$ m/s (*a*) and $V^M_{\max} = 3$ m/s (*b*), dispersion of velocity fluctuations is 1 m/s.

Conclusions

This paper presents the technique of visualization of the 2D velocity field in the atmosphere from coherent images of a fragment of the scattering layer illuminated by a laser. It is shown that the velocity field can be visualized based on displacements of large-scale intensity inhomogeneities of the speckle structure appearing in the optical image of the illuminated spot due to scattering of

laser radiation by scatterers moving in the atmosphere.

The iteration method of filtering of the small-scale speckle structure of intensity fluctuations in the image and the iterating procedure of visualization of the velocity field, based on processing of filtered images, are proposed. Examples of successful visualization are presented under the condition that the regular flow velocity exceeds the fluctuating component. The proposed technique of separation of large-scale intensity fluctuations is not efficient from the viewpoint of computational speed, as well as the method of visualization of the velocity field is not perfect from the viewpoint of technical realization, but they reflect the principle of the proposed method, which can be used in development of new devices for investigation of atmospheric phenomena and processes. Thus, for example, this method can be applied for visualization of vortices in airplane trails, where regular velocities approach 15–20 m/s, which far exceeds random velocity variations due to atmospheric turbulence.

Acknowledgements

This work was supported in part by the Russian Foundation for Basic Research (Projects No. 06-05-64445 and No. 06-05-96951-r-ofi) and Presidium of SB RAS (Interdisciplinary Integration Project No. 63).

References

1. M. Franson, *Laser Speckle and Applications in Optics* (Academic, New York, 1979).
2. P.A. Bakut, V.I. Mandrosov, I.N. Matveev, and N.D. Ustinov, *Theory of Coherent Images* (Radio i Svyaz', Moscow, 1987), 264 pp.
3. N.A. Fomin, *Speckle Photography for Fluid Mechanics Measurements* (Springer-Verlag, Berlin, 1998), 290 pp.
4. M. Raffel, C. Willert, and J. Kompenhans, *Particle Image Velocimetry: A Practical Guide* (Springer-Verlag, Berlin, 1998), 232 pp.
5. H.-E. Abbrecht, M. Borys, N. Damaschke, and C. Tropea, Laser Doppler and Phase Doppler Measurement Techniques. Series: Experimental Fluid Mechanics (Springer, Berlin, 2003), 738 pp.
6. M. Raffel, H. Richard, K. Ehrenfried, B. Van der Wall, C. Burley, P. Beaumier, K. McAlister, and K. Pengel, Experiments in Fluids **36**, 146–156 (2004).
7. V.A. Banakh, A.V. Falits, and T. Halldorsson, in: *Proc. 13-th Coherent Laser Radar Conf.* (2005), pp. 19–22.
8. V. Banakh, A. Falits, and T. Halldorsson, in: Lidar Technologies, Techniques, and Measurements for Atmospheric Remote Sensing II, Proc. SPIE **6367**, 121–128.
9. V.A. Banakh, Atmos. Oceanic Opt. **20**, No. 4, 271–274 (2007).
10. T. Halldorsson, A. Langmeier, A. Prucklmeier, V.A. Banakh, and A.V. Falits, Proc. SPIE **6522**, 65220A-1–65220A-9 (2006).
11. T. Halldorsson, A. Langmeier, A. Prucklmeier, V. Banakh, and A. Falits, Newsroom of SPIE 10.1117/2.1200706.0615 (invited paper).
12. J.W. Goodman, *Statistical Optics* (Wiley, New York, 1985), 256 pp.
13. D.H. Nelson, L.D. Walters, E.P. MacKerrow, M.J. Schmit, C.R. Quick, W.M. Porch, and R.R. Petrin, Appl. Opt. **39**, No. 12, 1857–1871 (2000).
14. V.A. Banakh and A.V. Falits, Proc. SPIE **4678**, 132–143 (2001).
15. A.S. Monin and A.M. Yaglom, *Statistical Fluid Mechanics: Mechanics of Turbulence,* Volume 2 (The MIT Press, 1971).
16. V.A. Banakh and A.V. Falits, Atmos. Oceanic Opt. **16**, No. 8, 649–651 (2003).
17. V.I. Klyatskin, Usp. Fiz. Nauk **173**, No. 7, 689–710 (2003).